J. Plasma Phys. (2021), *vol*. 87, 905870311
Published by Cambridge University Press
doi:10.1017/S0022377821000581

Kinetic-ballooning-mode turbulence in low-average-magnetic-shear equilibria

I.J. McKinney[1,†], M.J. Pueschel[2,3,4], B.J. Faber[1], C.C. Hegna[1], A. Ishizawa[5] and P.W. Terry[6]

[1]Department of Engineering Physics, University of Wisconsin-Madison, Madison, WI 53706, USA

[2]Eindhoven University of Technology, 5600 MB Eindhoven, The Netherlands

[3]Dutch Institute for Fundamental Energy Research, 5612 AJ Eindhoven, The Netherlands

[4]Institute for Fusion Studies, University of Texas at Austin, Austin, TX 78712, USA

[5]Graduate School of Energy Science, Kyoto University, Uji, Kyoto 611-0011, Japan

[6]Department of Physics, University of Wisconsin-Madison, Madison, WI 53706, USA

(Received 21 December 2020; revised 10 May 2021; accepted 18 May 2021)

Kinetic-ballooning-mode (KBM) turbulence is studied via gyrokinetic flux-tube simulations in three magnetic equilibria that exhibit small average magnetic shear: the Helically Symmetric eXperiment (HSX), the helical-axis Heliotron-J and a circular tokamak geometry. For HSX, the onset of KBM being the dominant instability at low wavenumber occurs at a critical value of normalized plasma pressure $\beta_{\mathrm{crit}}^{\mathrm{KBM}}$ that is an order of magnitude smaller than the magnetohydrodynamic (MHD) ballooning limit $\beta_{\mathrm{crit}}^{\mathrm{MHD}}$ when a strong ion temperature gradient (ITG) is present. However, $\beta_{\mathrm{crit}}^{\mathrm{KBM}}$ increases and approaches the MHD ballooning limit as the ITG tends to zero. For these configurations, $\beta_{\mathrm{crit}}^{\mathrm{KBM}}$ also increases as the magnitude of the average magnetic shear increases, regardless of the sign of the normalized magnetic shear. Simulations of Heliotron-J and a circular axisymmetric geometry display behaviour similar to HSX with respect to $\beta_{\mathrm{crit}}^{\mathrm{KBM}}$. Despite large KBM growth rates at long wavelengths in HSX, saturation of KBM turbulence with $\beta > \beta_{\mathrm{crit}}^{\mathrm{KBM}}$ is achievable in HSX and results in lower heat transport relative to the electrostatic limit by a factor of roughly five. Nonlinear simulations also show that KBM transport dominates the dynamics when KBMs are destabilized linearly, even if KBM growth rates are subdominant to ITG growth rates.

Key words: plasma instabilities, plasma nonlinear phenomena, fusion plasma

1. Introduction

The stellarator as a fusion reactor concept is qualitatively different from the tokamak due to the inherently three-dimensional nature of the magnetic field. This added flexibility allows the stellarator approach to circumvent the need for toroidal plasma current to provide the confining poloidal magnetic field, meaning stellarators are less prone to potentially destructive plasma-current-driven instabilities (Gates *et al.* 2018). One consequence of this improved magnetohydrodynamic (MHD) behaviour is the potential

† Email address for correspondence: imckinney@wisc.edu

for robust high-β operation, where $\beta = 8\pi p/B_0^2$ is the normalized plasma pressure, p is the electron pressure and B_0 is the magnetic field strength, without the danger of current-driven instabilities. Even in the absence of large-scale MHD instability, the system may exhibit small-scale kinetic ballooning modes (KBMs), which could conceivably drive large energy and particle fluxes and thus be problematic for high-β operation of stellarators (Ishizawa *et al.* 2013; Aleynikova & Zocco 2017; Aleynikova *et al.* 2018). The purpose of this work is to expand on previous analyses of KBM instability and turbulence by probing the properties of these modes in stellarator equilibria with low average magnetic shear $\hat{s} = -(r/\iota)\,\mathrm{d}\iota/\mathrm{d}r$, where ι is the rotational transform and r is a radial coordinate labelling flux surfaces. Low average magnetic shear $\hat{s}$ is a notable design feature of some classes of neoclassical-transport-optimized stellarators such as the Helically Symmetric eXperiment (HSX). A deeper understanding of KBM saturation in such configurations will aid in the optimization of low-$\hat{s}$ equilibria with respect to finite-β turbulent transport.

Neoclassical transport governs confinement in the classical stellarator. However, this issue can be quelled by ensuring that bounce-averaged particle excursions from a given flux surface during a banana orbit nearly vanish (Boozer 1983; Mynick 2006). There are a number of ways to reduce stellarator neoclassical transport to tokamak-like levels, such as quasi-symmetry (Nührenberg & Zille 1988; Rodríguez, Helander & Bhattacharjee 2020) or quasi-isodynamicity (Palumbo 1968; Mikhailov *et al.* 2002), both of which are subsets of quasi-omnigeneity (Hall & McNamara 1975; Yu Isaev *et al.* 2003). Magnetic configurations with sufficiently minimized neoclassical cross-field diffusion are dominated by anomalous transport (Canik *et al.* 2007; Hirsch *et al.* 2008; Wolf *et al.* 2019). Drift-wave turbulence is a primary candidate to explain anomalous transport in these configurations. Drift waves exist in a variety of types such as ion-temperature-gradient (ITG) modes (Rudakov & Sagdeev 1961; Horton, Choi & Tang 1981; Xanthopoulos & Jenko 2007; Mynick, Pomphrey & Xanthopoulos 2010; Xanthopoulos *et al.* 2014; McKinney *et al.* 2019), trapped-electron modes (Coppi 1965; Coppi, Rosenbluth & Sadgeev 1967; Kadomtsev & Pogutse 1971; Faber *et al.* 2015) or KBMs (Connor, Hastie & Taylor 1978; Tang 1978; Strauss 1979; Antonsen & Lane 1980; Kotschenreuther 1986; Pueschel, Kammerer & Jenko 2008; Pueschel & Jenko 2010; Aleynikova *et al.* 2018).

The KBMs are electromagnetic modes, as they require fluctuations in the magnetic field. Typically, the onset of KBM-driven turbulent transport is associated with breaching the ideal MHD ballooning stability boundary (Snyder 1999; Snyder *et al.* 1999; Pueschel *et al.* 2008; Pueschel & Jenko 2010). It has been shown that ion magnetic drifts can introduce an additional physical effect not present in simple MHD modelling in the small-perpendicular-wavelength limit (Kotschenreuther 1986; Aleynikova & Zocco 2017). Specifically, coupling between a KBM and thermal ions provides additional free energy to the mode. This resonant effect arises from non-adiabatic contributions to the ion density fluctuations in a kinetic treatment of the governing equations (Hirose, Zhang & Elia 1995; Hirose & Elia 1996). This effect can be qualitatively captured in a two-fluid treatment of the system, suggesting that the mode is of a reactive type since the kinetic treatment is unnecessary for qualitative purposes (Hirose & Elia 1996).

In the present work, the focus lies on the $\beta_{\mathrm{crit}}^{\mathrm{KBM}}$ value at which the KBM becomes the most unstable microinstability; for a discussion of different threshold definitions, see Pueschel *et al.* (2008). An analysis of various Wendelstein 7-X equilibria (Aleynikova *et al.* 2018), an optimized quasi-omnigenous stellarator, with respect to KBMs suggests both that, for sufficiently large β, peak KBM growth rates occur as $k_y \to 0$ for a number of physically relevant parameter regimes and that the critical β at which KBMs become unstable is of the order of $\beta_{\mathrm{crit}}^{\mathrm{KBM}} \approx 1\,\%$, depending on the specific equilibrium. It is

https://doi.org/10.1017/S0022377821000581 Published online by Cambridge University Press

also shown in the same analysis that, in low-average-magnetic-shear Wendelstein 7-X configurations, KBMs can be destabilized before the ideal MHD limit $\beta_{\mathrm{crit}}^{\mathrm{MHD}}$. As will be shown here, this KBM threshold can be much lower than the MHD threshold $\beta_{\mathrm{crit}}^{\mathrm{MHD}}$, with $\beta_{\mathrm{crit}}^{\mathrm{KBM}} \approx 0.2\,\%$ in the HSX (a quasi-helically symmetric stellarator) over a range of wavelengths, raising the possibility that such configurations exhibit poor KBM turbulence and confinement properties. However, it is shown here that the saturated nonlinear heat flux is greatly reduced relative to the electrostatic ITG case when $\beta > \beta_{\mathrm{crit}}^{\mathrm{KBM}}$. This implies that expectations based on linearly calculated $\beta_{\mathrm{crit}}^{\mathrm{KBM}}$ values, e.g. that nonlinear heat fluxes tend to increase for $\beta > \beta_{\mathrm{crit}}^{\mathrm{KBM}}$, do not accurately account for critical nonlinear dynamics.

With the goal of developing a better understanding of the relationship between the magnetic geometry and $\beta_{\mathrm{crit}}^{\mathrm{KBM}}$, the gyrokinetic turbulence code GENE is used here to perform electromagnetic nonlinear gyrokinetic local flux-tube simulations (Jenko 2000) (see http://www.genecode.org for code details and access). This paper is organized as follows. Section 2 introduces both the simulation framework for the present work and details regarding the three magnetic geometries. In § 3, linear and nonlinear electromagnetic simulations of KBMs and analyses thereof are presented. Section 4 shows the scaling of $\beta_{\mathrm{crit}}^{\mathrm{KBM}}$ with the average magnetic shear and the normalized ITG and the similarities in linear KBM results between HSX, Heliotron-J and a circular tokamak. Lastly, conclusions are given in § 5.

2. Simulation approach and magnetic geometries

The gyrokinetic code GENE (Jenko 2000) is used in this work to investigate KBM and ITG turbulence via flux-tube simulations of low-average-magnetic-shear equilibria, namely HSX, the helical-axis Heliotron-J (H-J) (Obiki *et al.* 2000) and a circular tokamak geometry. GENE solves a system of coupled equations that consists of the Vlasov equation, the Poisson equation and Ampère's law while taking advantage of the increased computational efficiency provided by gyro-averaging the orbits of charged particles in a strong magnetic guide field (Brizard & Hahm 2007). For the full set of equations, see Pueschel *et al.* (2011). GENE uses a five-dimensional phase space in which the coordinate system consists of the x (radial), y (binormal), z (parallel to $\boldsymbol{B}_0$), $v_\parallel$ (parallel velocity space) and μ (perpendicular velocity space) directions. There is both a box size L and a resolution N for each direction. For the nonlinear HSX calculation presented here, the resolutions, box sizes and hyperdiffusion coefficients are the following: $N_x = 128$, $N_y = 96$, $N_z = 512$, $N_{v\parallel} = 32$, $N_\mu = 8$, $L_y = 251.3\rho_s$ (corresponding to $k_y^{\min}\rho_s = 0.025$), $L_x = 217.6\rho_s$, $N_{\mathrm{pol}} = 4$, $D_z = 8$, and $D_{v\parallel} = 2$, where $\rho_s = c_s m_i/(eB)$ is the ion sound gyroradius, N_{pol} is the number of poloidal turns, D_z is the the parallel real-space hyperdiffusion coefficient and $D_{v\parallel}$ is the parallel velocity-space hyperdiffusion coefficient (Pueschel, Dannert & Jenko 2010). Numerical convergence studies were performed, including for N_{pol}, to ensure that results presented here are numerically converged. Due to the significant extent along the field line of the KBMs studied in this work, $N_{\mathrm{pol}} = 4$ is required to achieve convergence (Faber *et al.* 2018). If under-resolved in N_{pol}, artificial reinforcement of the KBMs via the parallel boundary condition is possible, yielding unphysical results. This is consistent with previous work regarding trapped-electron modes in HSX and with recent studies of a tokamak geometry (Faber *et al.* 2018; Ball, Brunner & Ajay 2020). Lastly, we do not include either parallel magnetic field fluctuations or collisions.

The MHD equilibrium solver VMEC (Hirshman, van Rij & Merkel 1986) is used to generate the HSX and H-J equilibria, which are subsequently processed using the GIST code (Xanthopoulos *et al.* 2009). The coordinates are centred at the specified normalized toroidal magnetic flux $s_0 = \Psi/\Psi(a) = (r/a)^2$, where $\Psi(a)$ is the toroidal flux at the plasma boundary and a is the effective minor radius. Details pertaining to the specifics of

https://doi.org/10.1017/S0022377821000581 Published online by Cambridge University Press

low-$\hat{s}$ flux-tube geometries can be found in Faber *et al.* (2018) and McKinney *et al.* (2019) (HSX) and in Ishizawa *et al.* (2017) (H-J). All three configurations have comparable values of the average magnetic shear $\hat{s}$ along any given field line. As will be shown in this work, the average magnetic shear plays a critical role in determining $\beta_{\rm crit}^{\rm KBM}$, beyond the threshold prediction from MHD.

The magnetic equilibria used in this work are as follows. HSX is a four-field-period stellarator, where the number of field periods is defined as the number of times the magnetic geometry repeats per one toroidal transit, with aspect ratio $A = R_0/a \approx 10$, where R_0 is the major radius, mean magnetic field $\langle B_0 \rangle \approx 1$ T and low average magnetic shear $\hat{s} \approx -0.05$ at $s_0 = 0.5$. The major radius R_0 (minor radius a) of HSX is approximately 1.2 m (0.12 m). The HSX flux tube used throughout this work is centred at the outboard midplane, corresponding to $\alpha = 0$, where $\alpha = \theta - \iota\zeta$ is a field-line label and θ and ζ are the poloidal and toroidal angles in PEST coordinates, respectively, where PEST coordinates are a straight field-line coordinate system (Grimm, Greene & Johnson 1976). It should also be noted that HSX is not optimized for a specific β, and therefore the HSX configuration used is given by the vacuum case with $\beta = 0$. This choice, however, is independent of the β used in GENE. Investigation into the effect of including self-consistent, finite equilibrium β values was performed, and it was found that changing the equilibrium β does not significantly affect the results presented below. Figure 4, a plot of growth rate and real frequency spectra of HSX using both a $\beta = 0$ equilibrium and a self-consistent $\beta = 0.48\,\%$ equilibrium, highlights that there is no significant difference between the vacuum and finite-β cases. As a result, the ∇B and curvature κ drifts are taken to be the same in this work, as is consistent with a $\beta = 0$ equilibrium. The H-J configuration used in this work has an equilibrium $\beta \approx 0.03\,\%$, four field periods, aspect ratio $A \approx 7.3$, mean magnetic field $\langle B_0 \rangle \approx 1.35$ T and average magnetic shear $\hat{s} \approx 0.028$, which is a factor of two smaller than that of HSX and of opposite sign, at $s_0 = 0.5$. The major radius R_0 (minor radius a) of H-J is 1.18 m (0.162 m). As was the case for HSX, the $\alpha = 0$ flux tube is employed for H-J in this work. It should be reiterated that H-J is not a quasi-symmetric stellarator. Lastly, an $\hat{s}$–α geometry, corresponding to a tokamak with circular flux surfaces, is used to investigate KBM dynamics in an axisymmetric system for comparison (Connor *et al.* 1978). A value of average magnetic shear $\hat{s} = -0.052$ is used throughout, as is a self-consistent (with β and the pressure gradients) $\alpha_{\rm MHD} = \iota^{-2}(R_0/L_n)[\beta_e(1+\eta_e) + \beta_i(1+\eta_i)]$, where L_n and $\eta_{(i,e)}$ are the density gradient scale length and the ratio of the (ion, electron) temperature gradient to the density gradient, respectively. It should be noted that since a negative value of $\hat{s}$ is used, this tokamak equilibrium is stable to ideal MHD ballooning, $\beta_{\rm crit}^{\rm MHD} \to \infty$ (Greene & Chance 1981; Antonsen *et al.* 1996).

3. Electromagnetic ITG and KBM turbulence

3.1. *Linear eigenmodes in low-$\hat{s}$ configurations*

Typically, as β increases, the normalized ITG growth rates γ in units of c_s/a, where c_s is the sound speed, steadily decrease (Pu & Migliuolo 1985; Dong, Guzdar & Lee 1987; Kim, Horton & Dong 1993). This is known as finite-β ITG stabilization, or linear electromagnetic stabilization. The mechanism by which this stabilization occurs is the coupling between the ITG mode and the shear Alfvén wave. This efficiently transfers energy out of the ITG mode, reducing its growth. Alterations of the ion Landau resonance due to finite-equilibrium-β ∇B modifications from the bending of perturbed field lines can also play a role in the stabilization (Jarmén, Anderson & Malinov 2015). This reduction

https://doi.org/10.1017/S0022377821000581 Published online by Cambridge University Press

in growth rate will tend to reduce the nonlinear heat flux, but additional physics can also have an impact on the dynamics.

Another mechanism that affects ITG transport levels as β increases is nonlinear electromagnetic stabilization (Pueschel *et al.* 2008; Pueschel & Jenko 2010; Whelan, Pueschel & Terry 2018; Whelan *et al.* 2019). As β increases, one observes a reduction in nonlinear heat flux that is greater than the reduction in linear growth rates or quasilinear fluxes. As has been shown in Whelan *et al.* (2018, 2019), the difference between the (quasi-)linear and nonlinear reduction stems from changes in the efficiency of zonal-flow-mediated energy transfer to stable modes. This effect has been shown to be active in a range of configurations, both of tokamak and of stellarator type. It has also been demonstrated that the inclusion of a self-consistent Shafranov shift can eliminate nonlinear electromagnetic stabilization for different, specific parameter regimes (Ishizawa *et al.* 2019).

The physical mechanism underlying KBM destabilization is the following. As with most microinstabilities, KBMs are destabilized when the driving force associated with the pressure gradient is sufficiently strong in the bad curvature region to overcome the stabilizing force from the magnetic field (Cheng 1982). More specific to KBMs, the modifications to magnetic drifts by β-induced magnetic fluctuations result in destabilizing effects when a kinetic treatment is applied to the governing equations. This is due to a resonance between the KBM and thermal ions, giving the KBM an additional free energy source.

For the cases studied here, the dominant eigenmode for $\beta < \beta_{\mathrm{crit}}^{\mathrm{KBM}}$ is ITG, whose growth rate decreases with β. For $\beta \geq \beta_{\mathrm{crit}}^{\mathrm{KBM}}$, KBM has a larger growth rate than the ITG mode with the growth rate increasing rapidly with β. This critical value $\beta_{\mathrm{crit}}^{\mathrm{KBM}}$ is generally of the order of 1 % in standard tokamaks and is comparable to the ideal MHD ballooning β limit for physically relevant gradient values (see Pueschel *et al.* 2008; Pueschel & Jenko 2010; Ishizawa *et al.* 2013). However, $\beta_{\mathrm{crit}}^{\mathrm{KBM}}$ is not always close to $\beta_{\mathrm{crit}}^{\mathrm{MHD}}$ and is, in general, a complicated function of the magnetic geometry.

Before presenting analyses of nonlinear simulations, the behaviour and scaling of linear instability will be elucidated, for both dominant and subdominant eigenmodes. Typically, ITG and KBM growth rates decrease and increase, respectively, as β increases. Figure 1 highlights this behaviour in HSX at normalized binormal wavenumber $k_y\rho_s = 0.6$. Henceforth, normalized wavenumbers are denoted $k_y\rho_s \rightarrow k_y$. The normalized gradients, β and the temperature ratio used in these calculations and throughout this work are $a/L_{Ti} = 3$ and $a/L_{Te} = a/L_n = 1$, $\beta = 0.48\,\%$ and $T_i/T_e = 1$, respectively, unless otherwise stated. Note the factor-of-three reduction in the ITG growth rate as β increases before the KBM becomes dominant. This significant reduction in ITG growth rate is not observed for all values of k_y, as evidenced by figure 2, where at $k_y = 0.1$ there is no significant reduction in γ before KBMs become dominant for either the $N_{\mathrm{pol}} = 1$ or the $N_{\mathrm{pol}} = 4$ case. This is partially due to the fact that, in the $k_y = 0.1$ case, the KBM becomes dominant at a small critical normalized plasma pressure $\beta_{\mathrm{crit}}^{\mathrm{KBM}} \approx 0.18\,\%$ versus $\beta_{\mathrm{crit}}^{\mathrm{KBM}} \approx 2.2\,\%$ for the $k_y = 0.6$ case. Also note that $N_{\mathrm{pol}} = 4$ is required to achieve convergence, as elongated eigenmodes can artificially self-reinforce via the parallel boundary condition.

The scaling of $\beta_{\mathrm{crit}}^{\mathrm{KBM}}$ with k_y is presented in figure 3 for both HSX (blue squares) and NCSX (black triangles), a quasi-axisymmetric stellarator configuration optimized for operation at $\beta \approx 4.2\,\%$ (Neilson, Zarnstorff & Lyon 2002) with $\hat{s} \approx -0.5$ at $s_0 = 0.5$. For HSX, $\beta_{\mathrm{crit}}^{\mathrm{KBM}}$ is small relative to the ideal MHD ballooning limit $\beta_{\mathrm{crit}}^{\mathrm{MHD}}$, and considerably smaller than the high-$\hat{s}$ NCSX analogue where $\beta_{\mathrm{crit}}^{\mathrm{KBM}}$ is comparable to $\beta_{\mathrm{crit}}^{\mathrm{MHD}}$. The normalized gradients and temperature ratio used in the NCSX calculations are the same as were used for HSX. The ideal ballooning limit $\beta_{\mathrm{crit}}^{\mathrm{MHD}}$ is also shown as a horizontal

https://doi.org/10.1017/S0022377821000581 Published online by Cambridge University Press

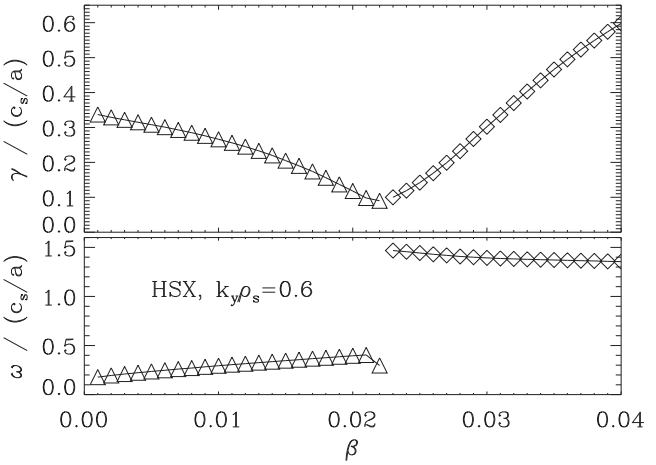

FIGURE 1. The growth rate and real frequency for the eigenmode with the largest growth rate at $k_y = 0.6$ over a range of β values for HSX with $a/L_{Ti} = 3$ and $a/L_{Te} = a/L_n = T_i/T_e = 1$. Note the stabilization of ITG growth rates (shown as triangles) as β increases and approaches $\beta_{\text{crit}}^{\text{KBM}} \approx 2.2\,\%$, where there is a clear discontinuity in real frequency, which highlights the change in dominant mode branch from ITG to KBM (shown as diamonds).

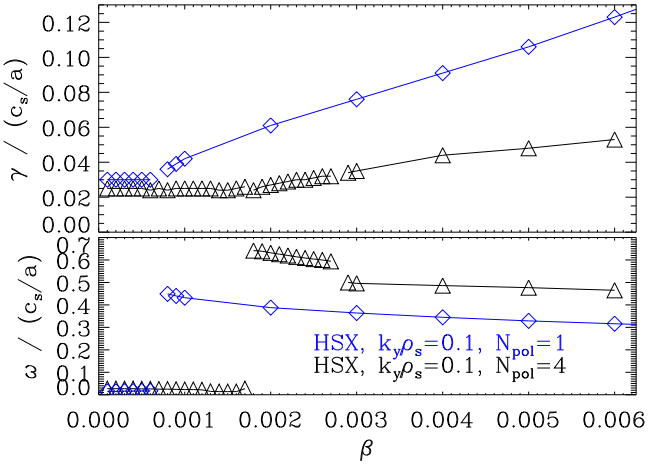

FIGURE 2. Growth rate and real frequency for $k_y = 0.1$ of the HSX configuration with $a/L_{Ti} = 3$ and $a/L_{Te} = a/L_n = T_i/T_e = 1$ for both $N_{\text{pol}} = 1$ (blue diamonds) and $N_{\text{pol}} = 4$ (black triangles). Note the lack of ITG stabilization relative to the $k_y = 0.6$ case and the significant difference between the two cases, an indication that $N_{\text{pol}} = 1$ is insufficient for convergence. Also, $\beta_{\text{crit}}^{\text{KBM}}$ is much lower for this case.

dashed line for each configuration. The NCSX curve smoothly approaches the MHD limit as k_y decreases until $k_y < 0.1$ where there is a slight uptick in $\beta_{\text{crit}}^{\text{KBM}}$. The HSX curve is well below the MHD limit in the transport-relevant $k_y < 0.25$ range, and dips to values $\approx 0.1\,\%$ that are an order of magnitude smaller than $\beta_{\text{crit}}^{\text{MHD}}$. This suggests that conditions in HSX are more conducive to KBM excitation due to ion kinetic physics (see § 4) than they are in NCSX. As will be shown, this is associated with the low average magnetic shear in HSX.

https://doi.org/10.1017/S0022377821000581 Published online by Cambridge University Press

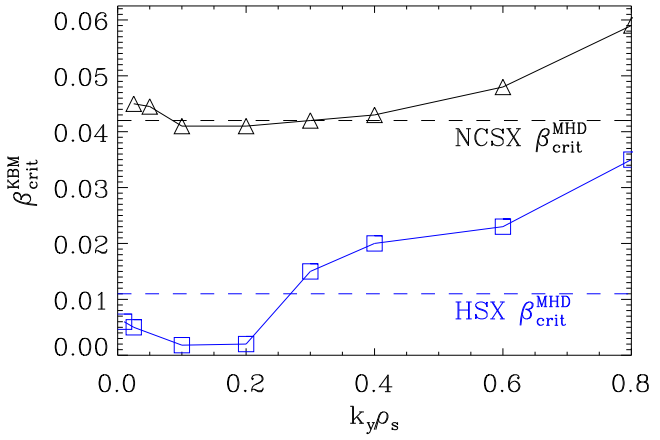

FIGURE 3. The $\beta_{\rm crit}^{\rm KBM}$ spectrum of NCSX (black triangles) and HSX (blue squares) with $a/L_{Ti} = 3$ and $a/L_{Te} = a/L_n = T_i/T_e = 1$. Horizontal dashed lines correspond to $\beta_{\rm crit}^{\rm MHD}$. Note the low $\beta_{\rm crit}^{\rm KBM}$ relative to $\beta_{\rm crit}^{\rm MHD}$ for HSX compared to NCSX.

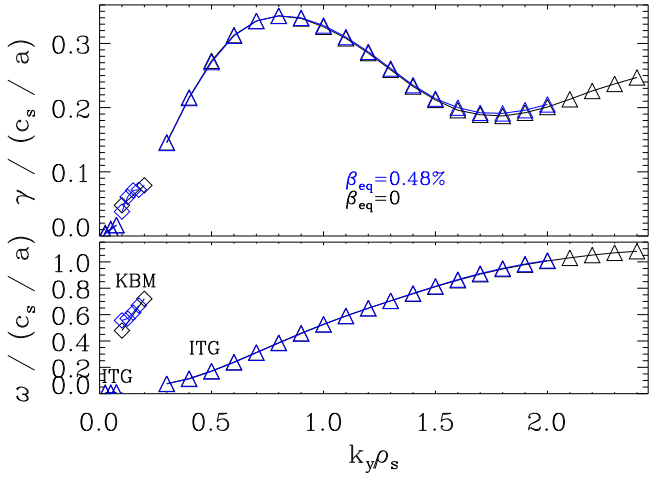

FIGURE 4. Growth rate and real frequency spectra for the HSX configuration (both with an equilibrium $\beta = 0$ (black) and equilibrium $\beta = 0.48\,\%$ (blue)) with $a/L_{Ti} = 3$, $\beta = 0.48\,\%$ and $a/L_{Te} = a/L_n = T_i/T_e = 1$. The KBMs (ITG modes) are denoted by diamonds (triangles). Note the transition from ITG to KBM (at roughly $k_y \approx 0.1$) and back to ITG (at roughly $k_y \approx 0.2$), highlighted by the discontinuity in real frequency. Also note the similarity in the two spectra when using a finite-β magnetic equilibrium versus using the vacuum case.

Figure 4 shows the dominant growth rates γ and real frequencies ω as functions of k_y at a constant $\beta = 0.48\,\%$. It is worth noting that KBM is dominant over a certain range of k_y values, namely $k_y \in [0.1, 0.2]$, while ITG is dominant over the remainder of the wavelength range. This means that nonlinear calculations of HSX at this value of β will potentially exhibit concurrent ITG and KBM drive characteristics, a phenomenon that is also observed in nonlinear simulations of tokamaks if $\beta \geq \beta_{\rm crit}^{\rm KBM}$ (Pueschel *et al.* 2008; Pueschel & Jenko 2010).

https://doi.org/10.1017/S0022377821000581 Published online by Cambridge University Press

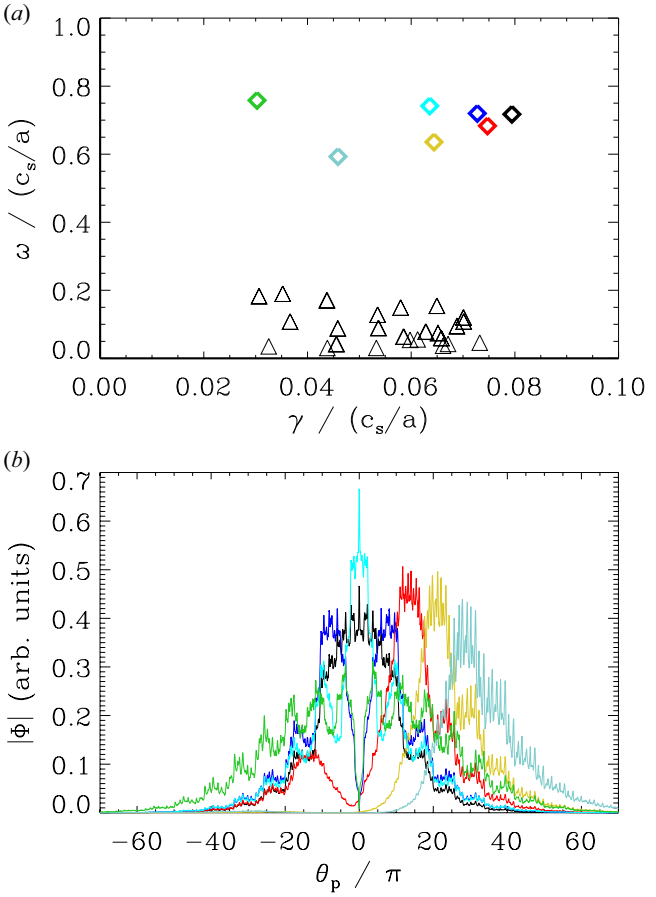

FIGURE 5. The subdominant spectrum (*a*) for HSX with $k_y = 0.2$ and $\beta = 0.5\,\%$ consisting of KBMs (diamonds) and ITG modes (triangles), and the associated electrostatic potential Φ eigenmode structures (*b*) for various KBMs. Note the two distinct families of KBMs: one with Φ symmetric about $\theta_p = 0$ and one with off-centre peaking. For each mode of the latter family, there is a sibling mode that is mirrored across the $\theta_p = 0$ axis with identical γ and ω; hence they are indistinguishable in (*a*). Also note that some of the centred KBMs (blue, green) have tearing parity, i.e. are odd functions of ballooning angle.

Lastly, the subdominant mode spectrum of HSX at $k_y = 0.2$ with $\beta = 0.5\,\%$, shown in figure 5, indicates that there is not just a single KBM that is destabilized as β increases, but rather there are two families of KBMs, one of which is a set of modes that are centred at the outboard midplane ($\theta_p = 0$) and another that consists of pairs of sibling modes that peak away from the outboard midplane ($\theta_p \neq 0$). It should be noted that some of the centred KBMs exhibit tearing parity (blue and green curves in figure 5*b*), i.e. the Φ eigenfunctions are odd in ballooning angle. The low background magnetic shear in the present scenario enables destabilization of these modes, termed tearing-parity KBMs, which had previously been conjectured not to exist based on a study involving high-shear equilibria (Pueschel *et al.* 2019). It is worth noting that it is unlikely that the tearing-parity KBMs discussed here are micro tearing modes because of the unique ITG dependence of the modes, the fact that the modes propagate in the ion diamagnetic direction and the relatively small electron thermal transport nonlinearly, three qualities that are not characteristic of micro

https://doi.org/10.1017/S0022377821000581 Published online by Cambridge University Press

tearing modes. For each mode that peaks away from the outboard midplane, a sibling mode exists with the same growth rate and frequency with an eigenmode structure that is near-perfectly mirrored with respect to $\theta_p = 0$. The physics implication of this is that HSX is qualitatively different from typical high-$\hat{s}$ tokamak cases, where only a single KBM is destabilized. Eigenvalue calculations with different gradients, $a/L_{Ti} = 4$ for example (with a/L_n and a/L_{Te} kept fixed), also exhibit the two branches of KBMs. However, the exact location of minimal $\beta_{\text{crit}}^{\text{KBM}}$ shifts in k_y space relative to the $a/L_{Ti} = 3$ case. The region of k_y space in which the outboard-midplane-peaked KBMs are dominant shifts to smaller k_y as ω_{Ti} increases. It should also be noted that the two branches of KBMs are robustly present when ensuring numerical convergence. This also complicates analysis of the nonlinear energy dynamics, as there may be a number of unstable KBMs involved in nonlinear energy transfer.

3.2. *Nonlinear characteristics of the ITG–KBM system*

Previous studies of KBM instability and turbulence have found critical β values of the order of one or a few per cent for experimentally relevant gradient values and magnetic geometries (Pueschel *et al.* 2008; Pueschel & Jenko 2010; Ishizawa *et al.* 2013). These analyses also show that for $\beta < \beta_{\text{crit}}^{\text{KBM}}$, the resulting turbulence is solely ITG or trapped-electron mode and for $\beta > \beta_{\text{crit}}^{\text{KBM}}$, signatures of multiple modes are present and observable in the simulations concurrently. Contrary to these cases, when $\beta > \beta_{\text{crit}}^{\text{KBM}}$, nonlinear simulations of the present HSX case do not achieve saturation when the minimum binormal wavenumber k_y^{min} of the system is unstable to KBMs. In such simulations, streamer modes span the length of the periodic radial domain, regardless of how large the radial box is, and self-reinforce via the radial periodic boundary condition of the flux tube. However, if one chooses k_y^{min} so that it is stable to KBMs, saturation can be achieved in electromagnetic flux-tube simulations, where a significant reduction in transport is observed relative to the near-electrostatic ($\beta = 0.05\,\%$) case. The time traces of heat flux (both ion electrostatic and electron electromagnetic) and particle flux for $k_y^{\text{min}} = 0.025$ are shown in figure 6. Despite the KBM being an electromagnetic mode, below the threshold it does not drive significant electromagnetic flutter heat transport given the choice of small electron temperature gradient $a/L_{Te} = 1$. While the condition that the smallest finite k_y must be KBM-stable is empirical, one possible underlying cause is the ability of the system to terminate an inverse cascade by means of ITG (stable) eigenmodes. The precise nature of the phenomenon is left for future study.

The heat flux spectrum given in figure 7 shows that the ion electrostatic heat flux $Q_i^{\text{es}}(k_y)$ peaks in the k_y range that is dominated by KBMs, consistent with the fact that β is roughly three times as large as $\beta_{\text{crit}}^{\text{KBM}}$ for $k_y = 0.1$. Figure 7 also shows that KBM transport is the dominant physics mechanism nonlinearly as long as KBMs are destabilized linearly, even if KBM growth rates are subdominant, where linear destabilization is shown in figure 4. As discussed above, k_y^{min} is sufficiently small that no KBM instability occurs at that mode; this is consistent with findings in high-$\hat{s}$ scenarios where nonlinear saturation is possible for β values up to $\beta_{\text{crit}}^{\text{KBM}}$ as $k_y \to 0$ (Pueschel & Jenko 2010). The nonlinear electrostatic potential Φ spectrum is depicted in figure 8, showing that the simulation is not dominated by a zonal flow, as the $k_y = 0.1$ non-zonal component of Φ is a factor of nearly two larger than the zonal component and the sum of the non-zonal contributions is significantly larger than the zonal contribution. This is an indication that zonal flows may play at most a minor role in saturation. This view is refined, however, based on nonlinear energy transfer analysis.

https://doi.org/10.1017/S0022377821000581 Published online by Cambridge University Press

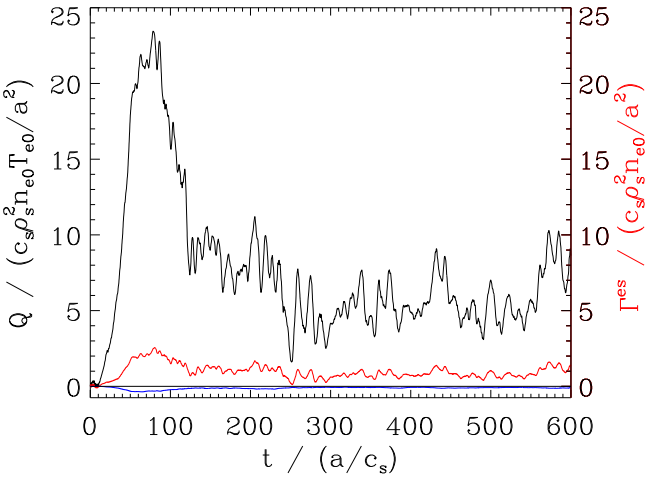

FIGURE 6. Heat (both ion electrostatic (black) and electron electromagnetic (blue)) and particle flux (red) time traces for HSX with $k_y^{\min} = 0.025$ and $\beta = 0.48\,\%$. There is a significant (factor of ≈ 5) reduction in $Q_i^{\rm es}$ relative to the near-electrostatic ($\beta \approx 0.05\,\%$) case (McKinney *et al.* 2019). There is negligible, slightly negative magnetic flutter transport, a result of the low electron temperature gradient $a/L_{Te} = 1$.

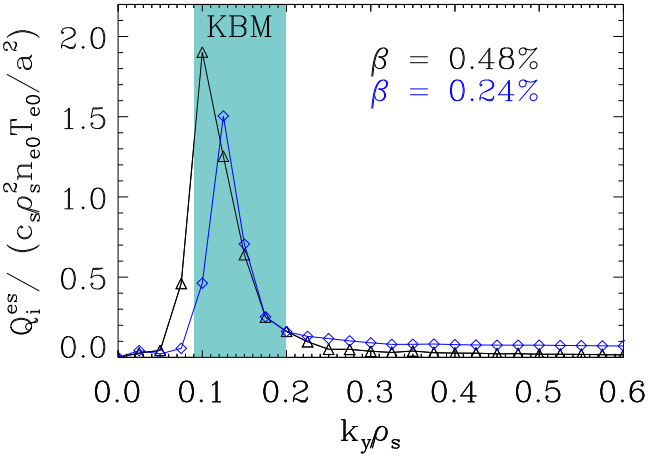

FIGURE 7. Heat flux spectra for HSX with $k_y^{\min} = 0.025$ and $\beta = 0.48\,\%$ (black) associated with the time trace shown in figure 6 and with $k_y^{\min} = 0.025$ and $\beta = 0.24\,\%$ (blue) for comparison. Note that the peaks of the spectra are almost fully contained in the binormal wavelength range over which KBM is destabilized, which is denoted by the shaded region. This shows that KBM transport dominates nonlinearly when KBMs are linearly destabilized, even if KBM growth rates are subdominant to ITG growth rates.

Nonlinear frequencies are shown in figure 9. Interestingly, there is no discontinuity in the nonlinear frequency spectrum of the HSX configuration, a feature that was present linearly at the ITG–KBM transition points in figure 4. Both dominant and subdominant linear KBM frequencies are overlaid in figure 9 to facilitate comparison with the nonlinear data. Clearly, throughout the range where linear data are shown, nonlinear frequency signatures match the values associated with the dominant outboard-centred KBMs. An exact

https://doi.org/10.1017/S0022377821000581 Published online by Cambridge University Press

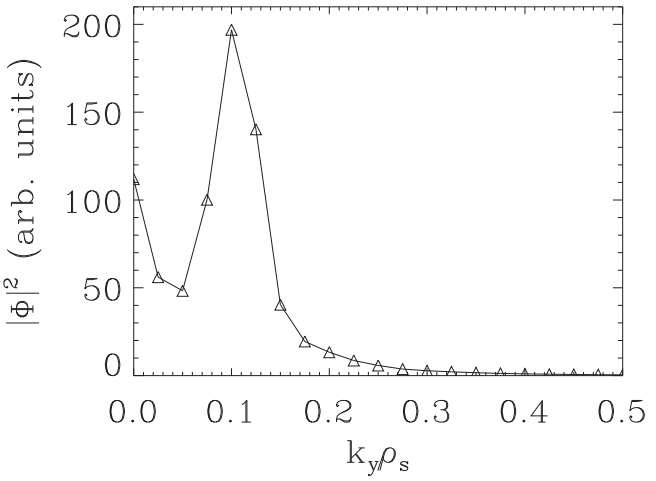

FIGURE 8. The nonlinear Φ spectrum for HSX with $k_y^{\min} = 0.025$ and $\beta = 0.48\,\%$. The spectrum is truncated at $k_y\rho_s = 0.5$ since $|\Phi|^2$ amplitudes are negligible above this threshold. Note that the zonal component is much weaker than the integrated non-zonal amplitudes.

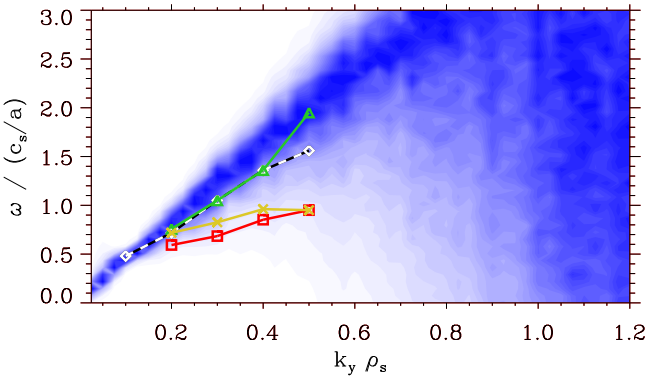

FIGURE 9. The nonlinear frequency spectrum for HSX with $k_y^{\min} = 0.025$ and $\beta = 0.48\,\%$. The colour scale has arbitrary units and is linear and normalized at each k_y separately. Linear frequencies of the most unstable (gold crosses), maximal-frequency (green triangles), minimal-frequency (red squares) and most unstable outboard-centred (black–white dashed diamonds) KBMs are also included for comparison. Note the agreement between the dominant linear outboard-centred KBM frequencies and the nonlinear signal.

frequency match is not expected to occur, as turbulence may result in a k_y-dependent nonlinear frequency shift and broadening. This constitutes evidence that KBMs do indeed play an important role in the nonlinear turbulent state.

Analysis of the nonlinear energy transfer to a given (k_x,k_y) point in Fourier space due to interaction with (k_x',k_y') and $(k_x - k_x', k_y - k_y')$ also suggests that modes in the KBM-dominated k_y range play an important role in the energy transfer dynamics of the turbulence and therefore in the dynamics that leads to saturation. Figure 10 shows nonlinear energy transfer at a given $(k_x = 0.06, k_y = 0.1)$, denoted by the tip of the black arrow, to and from various (k_x', k_y'). Regions of blue correspond to locations which cause energy input into $(k_x = 0.06, k_y = 0.1)$ while red regions correspond to locations which

https://doi.org/10.1017/S0022377821000581 Published online by Cambridge University Press

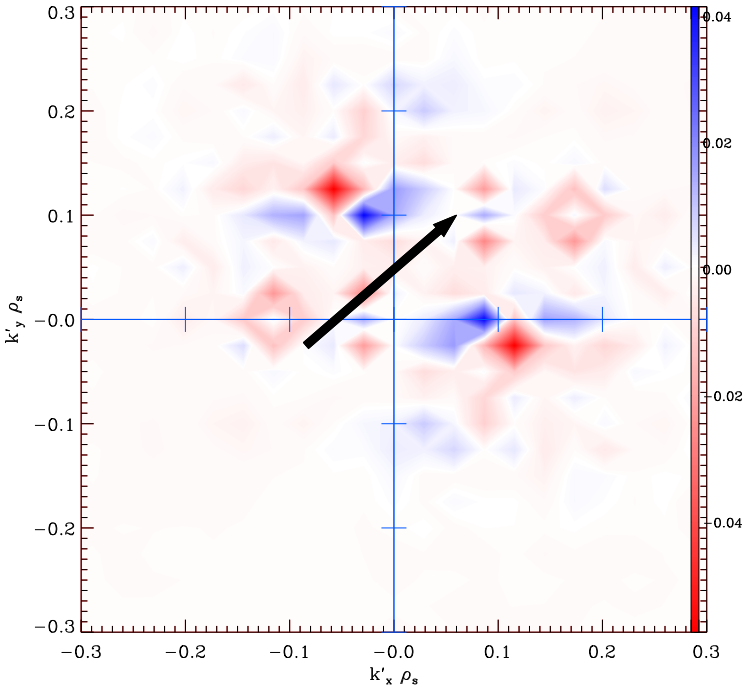

FIGURE 10. Nonlinear energy transfer functions indicate locations which give (blue) and receive (red) energy to and from ($k_x = 0.06$, $k_y = 0.1$), denoted by the tip of the black arrow. There is significant zonal transfer from ($k_x = 0.06$, $k_y = 0.1$) to the blue clouds near $k'_y = 0$ and $k'_y = 0.1$. Significant non-zonal energy transfer is also observed at $k'_y = -0.025$ and $k'_y = 0.125$.

draw energy from ($k_x = 0.06$, $k_y = 0.1$). The dominant method by which ($k_x = 0.06$, $k_y = 0.1$) receives energy is zonal energy transfer, indicated by the blue clouds at both $k'_y = 0$ and $k'_y = 0.1$. There is also significant non-zonal energy transfer via ($k'_x = 0.12$, $k'_y = -0.025$). It is important to note both that the largest energy sinks are due to non-zonal transfer and that the largest energy sinks are even larger than the largest energy inputs from zonal transfer. Lastly, the zonal energy transfer can occur due to both the zonal flow and the zonal field, i.e. the zonal component of the fluctuating magnetic field.

This result appears to contradict the earlier finding in figure 8 that the zonal-flow amplitudes are low. However, when coupling is sufficiently resonant, zonal flows can very efficiently mediate energy transfer even if they are only excited to low amplitudes.

Further analysis of nonlinear energy transfer yields insight into the wavelength ranges which dominate energy transfer between the turbulence and the zonal ($k_y = 0$) modes. Figure 11 shows normalized nonlinear energy transfer corresponding to $k_y = 0$ modes summed over both k_x and k'_x versus k'_y. The peak of the data occurs at $k'_y = 0.125$, well within the KBM-dominated k_y range. A significant portion of the energy transfer to and from zonal modes is facilitated by modes in the KBM-dominated k_y range, constituting additional evidence that KBMs are important nonlinearly. One can also construct a quantity to gauge the relative importance of a given k_y in the overall nonlinear energy transfer dynamics, as highlighted by figure 12, a plot of averaged nonlinear energy transfer functions versus k_y. This quantity is the sum (over $k_x \neq 0$) of the root mean squares (of each k'_x–k'_y plane) of the nonlinear energy transfer functions corresponding to a given (k_x,k_y). Both the zonal modes and KBMs contribute to the overall nonlinear energy transfer

https://doi.org/10.1017/S0022377821000581 Published online by Cambridge University Press

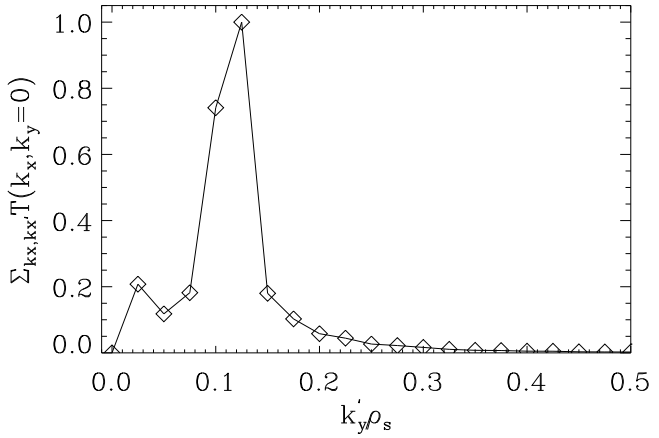

FIGURE 11. The sum (over $k_x \neq 0$) of the root mean squares (over coupled k'_x) of time-averaged nonlinear energy transfer functions for zonal ($k_y = 0$) modes as a function of k'_y. The data are normalized to the value of the point at $k'_y = 0.125$. Note that the peak is in the KBM-dominated k'_y range, evidence that KBMs play an important role in zonal dynamics.

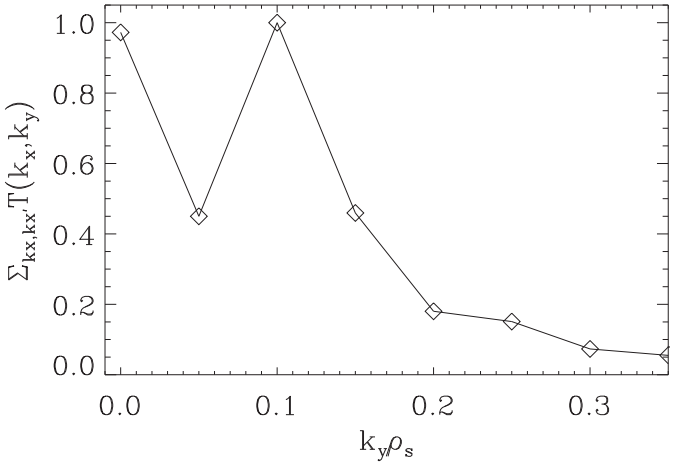

FIGURE 12. The sum (over $k_x \neq 0$) of the root mean squares (over coupled k'_x, k'_y) of time-averaged nonlinear energy transfer functions, which are normalized by the value of the same quantity at $k_y = 0.1$.

dynamics, with KBMs contributing roughly twice as much if one integrates over the entire KBM-dominated k_y range.

Lastly, figure 13 shows both the electrostatic ion heat and particle fluxes as β increases. Simulations with $k_y^{\min} = 0.025$ for $\beta = 0.75\,\%$ and $1\,\%$ grow without bounds and therefore do not have associated data points. This is consistent with the requirement that $k_y^{\min}$ be stable to KBMs for saturation to occur, as $\beta_{\rm crit}^{\rm KBM} \approx 0.6\,\%$ for $k_y = 0.025$, as shown in figure 3. Note the decrease in heat flux as β increases until β is sufficiently close to $\beta_{\rm crit}^{\rm KBM}(k_y^{\min})$, a result that is consistent with ITG nonlinear finite-β stabilization. The uptick in $Q_i^{\rm es}$ as β increases from $0.48\,\%$ to $0.55\,\%$ is an expression of the KBMs, which, unlike the ITG modes, become more virulent as β is increased.

https://doi.org/10.1017/S0022377821000581 Published online by Cambridge University Press

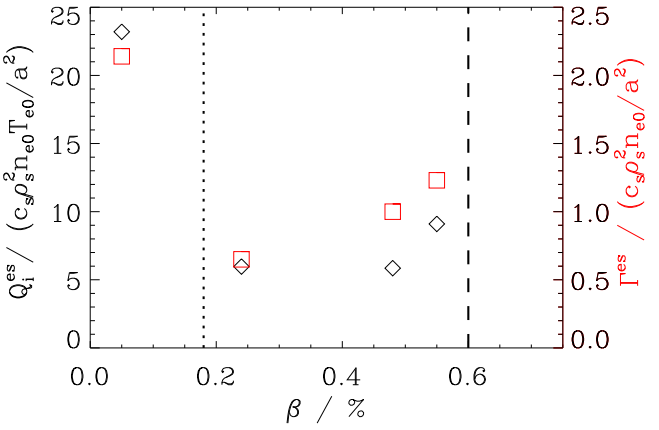

FIGURE 13. Normalized ion heat flux Q_i^{es} (black diamonds) and particle flux Γ^{es} (red squares) as a function of β. Observe the significant reduction of transport for $\beta \gtrsim 0.2\,\%$ relative to $\beta \approx 0.05\,\%$ until β approaches the $\beta_{\mathrm{crit}}^{\mathrm{KBM}} \approx 0.6\,\%$ threshold for $k_y = 0.025$. Above $\beta = 0.6\,\%$, simulations no longer achieve a saturated state. The vertical dashed black line indicates $\beta_{\mathrm{crit}}^{\mathrm{KBM}} = 0.6\,\%$ at $k_y = 0.025$ and the vertical dotted black line indicates $\beta_{\mathrm{crit}}^{\mathrm{KBM}} = 0.18\,\%$ at $k_y = 0.1$. The electron electromagnetic heat flux is negligible (normalized $Q_e^{\mathrm{em}} \approx -0.2$ for $\beta = 0.48\,\%$) and therefore not included in this analysis.

4. Impact of average magnetic shear and ITG

Further investigation demonstrates that $\hat{s}$ and a/L_{Ti} are particularly important in setting the value of $\beta_{\mathrm{crit}}^{\mathrm{KBM}}$ relative to the ideal ballooning threshold. This section addresses how the linear KBM characteristics presented in § 3 change as both the average magnetic shear $\hat{s}$ and the fractional component of the total pressure gradient a/L_p driven by the ITG a/L_{Ti} change. Linear results pertaining to H-J and a circular geometry with low $\hat{s}$ are also shown.

Figure 14 presents $\beta_{\mathrm{crit}}^{\mathrm{KBM}}$ as a function of $\hat{s}$ and demonstrates that the KBM threshold increases with $|\hat{s}|$, regardless of sign. This is consistent with the observations that, in general, drift waves are commonly stabilized by increased $|\hat{s}|$ (Pearlstein & Berk 1969; Ross & Mahajan 1978). Modification of the average magnetic shear of the flux tube is done self-consistently in the sense that the derivative of ι is adjusted to yield the desired $\hat{s}$ and then geometric elements are recalculated accordingly. Furthermore, eigenvalue calculations of HSX with artificially high $\hat{s}$ yield a subdominant mode spectrum that corresponds to the usual tokamak, single-unstable-KBM scenario, as well as to the NCSX configuration discussed in § 3.1. The physics implication of this result is that with increased shear, modes are less extended along the magnetic field line and therefore cannot access free energy in gradients via the bad curvature regions further along the field line, as evidenced by figure 15, a plot of two characteristic Φ eigenmodes for the $\hat{s} = -0.05$ case (black) and the $\hat{s} = 0.5$ case (blue). Conversely, KBMs are therefore more easily destabilized with more free energy to access when $|\hat{s}|$ is low like in HSX.

This result is consistent with previous work investigating KBM behaviour in low-magnetic-shear tokamaks (Hirose *et al.* 1995; Hirose & Elia 1996; Zonca *et al.* 1999). In Hirose & Elia (1996), despite low negative $\hat{s}$, which implies stability with respect to ideal MHD ballooning modes, one observes KBMs at relatively small critical $\beta_{\mathrm{crit}}^{\mathrm{KBM}} \approx 0.5\,\%$ with $\hat{s} = -0.2$ and $k_y = 0.1$ when a sufficiently strong ITG is present. It has been suggested that the cause of this destabilization of KBMs at small β is an effect of ion magnetic drift resonance (Hirose *et al.* 1995; Hirose & Elia 1996; Chen *et al.* 2018).

https://doi.org/10.1017/S0022377821000581 Published online by Cambridge University Press

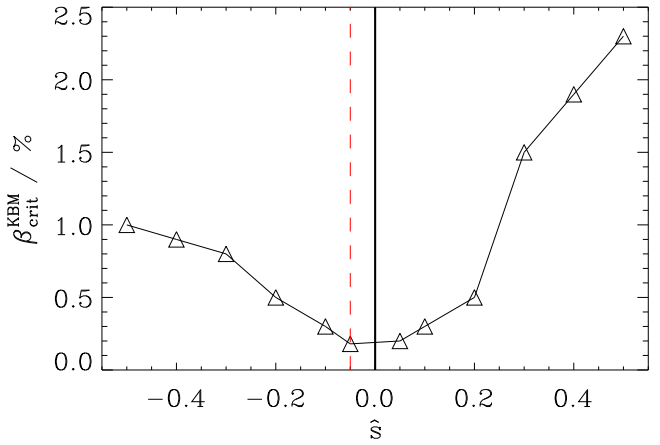

FIGURE 14. The $\beta_{\rm crit}^{\rm KBM}$ as a function of $\hat{s}$ for the HSX configuration with $k_y = 0.1$. The vertical dashed red line highlights the self-consistent nominal $\hat{s}$ for HSX at $s_0 = 0.5$. Note that $\beta_{\rm crit}^{\rm KBM}$ increases as the magnitude of the average magnetic shear increases, regardless of sign.

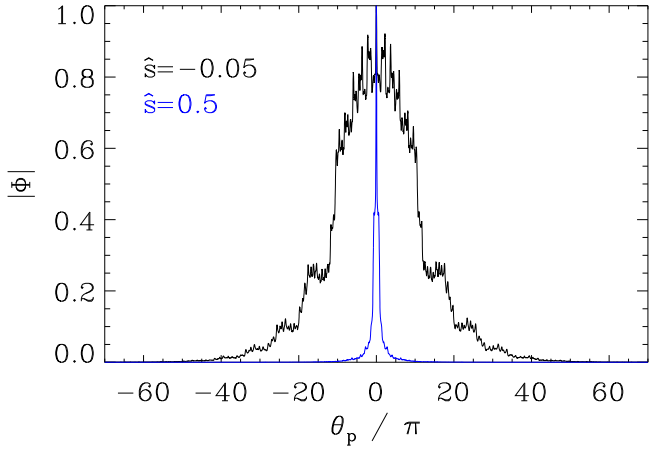

FIGURE 15. Characteristic Φ eigenmode structures for KBMs for the HSX geometries with $\hat{s} = -0.05$ (black) and $\hat{s} = 0.5$ (blue) which highlight the extended nature of the eigenmodes when the magnitude of the average magnetic shear is low. The mode structure magnitudes are normalized to their values at the outboard midplane.

Thermal ions couple to and exchange energy with the drift wave via the geodesic curvature of the magnetic geometry. There are also recent reports of KBMs in experiments which exhibit low negative magnetic shear (Chen *et al.* 2016, 2018), where it is suggested that the same ion-magnetic-drift effect is responsible for the destabilization at small β.

A preliminary, lowest-order analysis of the ion-magnetic-drift resonance condition, derived using a two-fluid model that accounts for kinetic effects, given in Hirose & Elia (1996):

$$(\omega - 5/3\,\omega_{Di})^2 - 10/9\,\omega_{Di}^2 = 0, \tag{4.1}$$

where $\omega_{Di} = 2cT_i/(eB^3)(\nabla B \times \boldsymbol{B}) \cdot \boldsymbol{k}_\perp$, suggests that the KBM frequencies observed in the present work exhibit good agreement with that required for exact resonance. Note the different sign used in the parentheses in (4.1) due to the difference in sign convention

https://doi.org/10.1017/S0022377821000581 Published online by Cambridge University Press

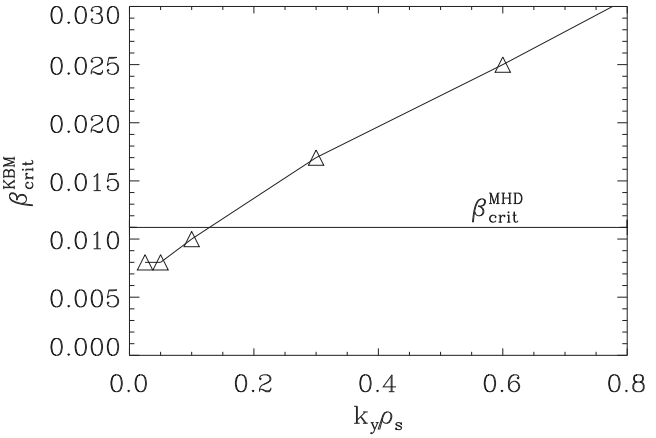

FIGURE 16. The $\beta_{\rm crit}^{\rm KBM}$ spectrum for HSX with a stronger density gradient contribution compared with figure 3: $a/L_n = 2.5$, $a/L_{Ti} = 0$ and $a/L_{Te} = 1$. Since two particle species are used, the sum of the gradients is $2.5 + 2.5 + 1 = 6$, which is equal to the sum of the gradients in figure 3. Note that the KBM limit is now closer to $\beta_{\rm crit}^{\rm MHD}$ as $k_y \to 0$.

used for ω here relative to Hirose & Elia (1996). Taking $T_e/T_i = 1$, $2cT_i/(eB) \to c_s\rho_s$ and $\nabla B \to B/a$, the ion-magnetic-drift frequency can be written as $\omega_{Di}/(c_s/a) \approx k_\perp\rho_s$. After computing an eigenmode average for $k_\perp\rho_s$ which accounts for geometry, given by

$$\langle k_\perp\rho_s\rangle = \frac{\int |\Phi|^2((k_x\rho_s)^2 g^{xx} + 2k_xk_y\rho_s^2 g^{xy} + (k_y\rho_s)^2 g^{yy})^{1/2}\,{\rm d}\theta_p}{\int |\Phi|^2\,{\rm d}\theta_p}, \tag{4.2}$$

where g^{xx}, g^{xy} and g^{yy} are magnetic geometry elements, $\omega_{Di}/(c_s/a) \approx \langle k_\perp\rho_s\rangle$ yields a normalized ion-magnetic-drift frequency $\omega_{Di} = 0.266$ for $(k_x = 0,\ k_y = 0.2)$. Using this value for ω_{Di}, one can evaluate (4.1) to determine the resonant mode frequency. The resonant frequency is $\omega \approx 0.724$ for $(k_x = 0, k_y = 0.2)$. The resonant frequency calculated here is in agreement with the dominant KBM real frequency in figure 4 at $k_y = 0.2$, where $\omega_r \approx 0.72$. This constitutes quantitative evidence that the ion-magnetic-drift resonance is likely playing an important role in the dynamics. A more thorough analysis of the ion-magnetic-drift resonance phenomenon will be left to future work.

In support of the concept that ion dynamics is of particular importance to KBM behaviour in HSX geometry, figure 16 shows $\beta_{\rm crit}^{\rm KBM}$ as a function of k_y, similar to figure 3, but with different gradients. Keeping the sum of the gradients as well as a/L_{Te} constant, setting $a/L_{Ti} = 0$ and increasing a/L_{Tn} accordingly, one observes both a roughly five-fold increase in $\beta_{\rm crit}^{\rm KBM}$ at $k_y = 0.1$ and that $\beta_{\rm crit}^{\rm KBM}$ no longer dips as far below $\beta_{\rm crit}^{\rm MHD}$. Below $k_y = 0.025$, $\beta_{\rm crit}^{\rm KBM}$ is difficult to ascertain, as a mode that drifts in the electron diamagnetic direction with even Φ parity and odd $A_\parallel$ parity dominates over the relevant β range and eigenvalue calculations are impractical at such small values of k_y. This result constitutes further evidence that ion dynamics is of particular importance to KBM behaviour in HSX.

Regarding scalings of KBM turbulence and confinement at high β, linear computations alone are often insufficient to predict nonlinear trends, particularly at low $\hat{s}$, as discussed in, for example, Hegna, Terry & Faber (2018) and McKinney *et al.* (2019). While more research on this topic in the context of KBMs is required, the low heat fluxes in figure 6 show both that the strong linear KBM drive at low magnetic shear does not produce

https://doi.org/10.1017/S0022377821000581 Published online by Cambridge University Press

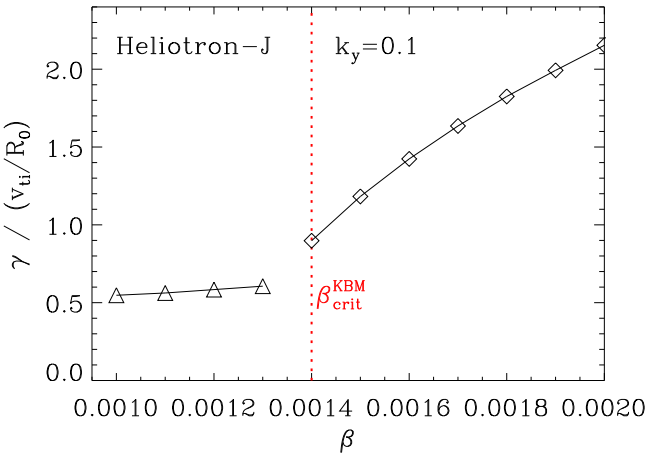

FIGURE 17. Growth rate γ as a function of β for H-J at $k_y = 0.1$ with the following normalized (to major radius) gradients: $R_0/L_{Ti} = 13$, $R_0/L_{Te} = 17$ and $R_0/L_n = 9.3$. The ITG modes (triangles) dominate below $\beta_{\rm crit}^{\rm KBM}$ and KBMs (diamonds) dominate above $\beta_{\rm crit}^{\rm KBM}$. Note that $\beta_{\rm crit}^{\rm KBM} = 0.14\,\%$, shown in red, is comparable to that for HSX for the same binormal wavenumber.

corresponding fluxes and that electromagnetic stabilization of the heat flux relative to the electrostatic case can be shown. More explicitly, dominant linear growth rates alone are poor predictors of nonlinear heat fluxes at finite β.

Analyses similar to the ones conducted above for HSX were also carried out for both H-J and a circular axisymmetric geometry. The H-J case, a configuration with similarly low average magnetic shear ($\hat{s} \approx 0.028$), also exhibits a small $\beta_{\rm crit}^{\rm KBM} \approx 0.14\,\%$ at $k_y = 0.1$, as evidenced by figure 17. This value of $\beta_{\rm crit}^{\rm KBM}$ verifies calculations carried out using the GKV code of the same H-J equilibrium using the same gradient values (Maeyama *et al.* 2013; Ishizawa *et al.* 2017). Also note that there is a slight increase in the ITG growth rates as $\beta \to \beta_{\rm crit}^{\rm KBM}$, i.e. no linear electromagnetic stabilization occurs. One particular benefit of including H-J in this analysis is to highlight the fact that the linear and nonlinear KBM dynamics observed numerically in HSX are not simply the product of an aspect of the magnetic geometry that is unique to HSX, but rather are indicative of KBM behaviour in a broader class of magnetic equilibria which exhibit small average magnetic shear.

A shifted-circle tokamak geometry with a low negative average magnetic shear $\hat{s} \approx -0.05$ also exhibits $\beta_{\rm crit}^{\rm KBM}$ spectra and eigenvalue characteristics similar to those for HSX, as shown in figure 18. Note the similarities in the $\beta_{\rm crit}^{\rm KBM}$ spectrum between HSX and the circular tokamak with low negative average magnetic shear. Both curves are non-monotonic and have a minimum at $k_y = 0.1$ with a very small critical $\beta_{\rm crit}^{\rm KBM} \approx 0.1\,\%$, as shown in figure 18(*a*). It is also worth noting that the low-k_y behaviour of $\beta_{\rm crit}^{\rm KBM}$ in s–α is insensitive to the use of a self-consistent equilibrium relative to the high-k_y behaviour. The subdominant mode landscape for the circular tokamak is also qualitatively consistent with the HSX results, as two distinct clouds of modes are present, an ITG and a KBM branch, as shown in figure 18. However, one key difference between the subdominant mode spectra for HSX and the circular tokamak is the presence of only a single ballooning-parity and tearing-parity KBM branch for the circular tokamak case. The single KBM branch in the axisymmetric case resembles the branch of KBMs centred at the outboard midplane for HSX.

https://doi.org/10.1017/S0022377821000581 Published online by Cambridge University Press

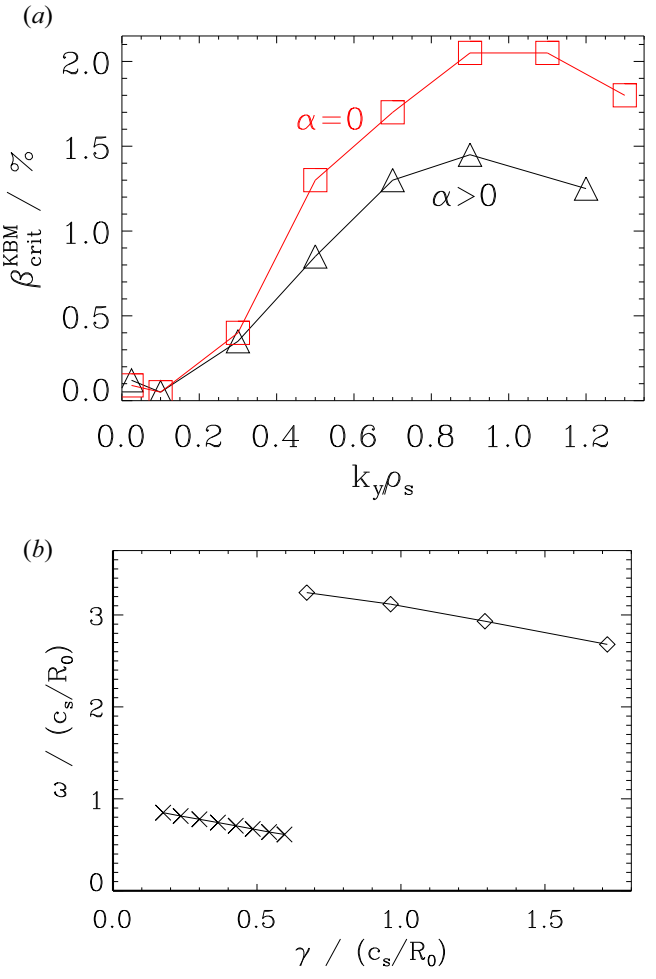

FIGURE 18. The β_{crit}^{KBM} spectrum (*a*) and the subdominant mode spectrum at $k_y = 0.2$ and $\beta = 0.8\,\%$ (*b*) for an $\hat{s} = -0.052$ circular tokamak (*s*–α) geometry. (*a*) There are two curves: one for the case when $\alpha_{MHD} = 0$ (red squares), where the equilibrium and GENE β are not self-consistent; and a second for the case when α_{MHD} is such that both the equilibrium and GENE β are the same (black triangles). (*b*) The two distinct subdominant ITG (crosses) and KBM (diamonds) clouds are also present in the circular tokamak case. However, there is only a single KBM branch in this case versus the two that were present in HSX.

In summary, both H-J and a circular axisymmetric geometry with $\hat{s} \approx -0.05$ exhibit KBM behaviour similar to that in HSX, providing strong evidence that the relatively weak averaged magnetic shear is an important factor in determining the KBM dynamics.

5. Conclusions

Gyrokinetic electromagnetic simulations of HSX, H-J and a circular tokamak have been presented, showing that KBMs can be excited at a critical β_{crit}^{KBM} that is considerably smaller than the critical β for ideal MHD ballooning. This difference is associated with the relatively low average magnetic shear of these configurations. While one might expect this to bode poorly for the performance of low-average-shear magnetic equilibria, nonlinear

https://doi.org/10.1017/S0022377821000581 Published online by Cambridge University Press

simulations of HSX show that saturation is achievable with $\beta_{\text{crit}}^{\text{KBM}} < \beta < \beta_{\text{crit}}^{\text{MHD}}$ and that a significant reduction in transport is observed relative to the $\beta \approx 0$ case. However, saturation only occurs when the minimum binormal wavenumber $k_y^{\text{min}}\rho_s$ of the system is stable to KBMs. One possible explanation of this result is that the nonlinear transfer of energy from the strongly driven KBMs in the binormal wavenumber range $0.1 < k_y\rho_s < 0.2$ to stable modes with $k_y\rho_s < 0.1$ in Fourier space is possible and allows for saturation when the condition that $k_y^{\text{min}}\rho_s$ is stable to KBMs is met.

The KBM subdominant mode spectrum of HSX is qualitatively different from what one would observe in an $\hat{s} \sim 1$ tokamak, as HSX exhibits two families of unstable KBMs, whereas there is generally only a single unstable KBM in the high-$\hat{s}$ tokamak case. With low $\hat{s}$, KBMs are more extended along the field line, allowing such modes to access free energy in the gradients via the bad curvature regions away from the outboard midplane of a given field line. As a consequence, KBMs can peak at finite ballooning angle, and even tearing-parity KBMs (TKBMs in the nomenclature of Pueschel *et al.* (2019)) are found. With respect to $\hat{s}$, $\beta_{\text{crit}}^{\text{KBM}}$ increases monotonically, regardless of the sign of the average magnetic shear. This is consistent with the fact that stronger magnetic shear tends to stabilize drift waves.

A number of nonlinear analyses have also been conducted here which highlight the importance of KBMs in the nonlinear dynamics. Heat flux spectra shown in figure 7 highlight that KBM transport dominates the dynamics when KBMs are destabilized linearly, even if KBM growth rates are subdominant to ITG growth rates. A comparison of dominant linear KBM real frequencies and nonlinear frequencies shows good agreement in the KBM-dominated k_y range. This constitutes evidence that KBMs are significantly contributing to the nonlinear state. Additionally, an analysis of nonlinear energy transfer shows that KBMs play an integral role in the energy transfer dynamics, even more so than zonal modes, further highlighting the fact that the nonlinear state indeed shows signs of both ITG and KBM drive. An investigation of how the electrostatic ion heat flux changes as a function of β shows a decrease in heat flux as β increases until β is sufficiently close to $\beta_{\text{crit}}^{\text{KBM}}(k_y = k_y^{\text{min}})$, showing both the improved nonlinear behaviour relative to linear $\beta_{\text{crit}}^{\text{KBM}}$ predictions and the steep increase in fluxes at large values of $\beta \gg \beta_{\text{crit}}^{\text{KBM}}$.

The linear characteristics of the low-average-magnetic-shear equilibria presented in this work raise questions regarding the utility of such configurations at the β values required for an efficient fusion reactor concept. However, as the nonlinear calculations presented here show, nonlinear dynamics can overcome poor linear KBM properties such as the increase in total heat flux generally associated with $\beta > \beta_{\text{crit}}^{\text{KBM}}$, and nonlinear fluxes in HSX even decrease as β increases above $\beta_{\text{crit}}^{\text{KBM}}(k_y = 0.1)$, as shown in figure 13, until $\beta \approx 0.6\,\%$. It is important to keep such KBM saturation physics in mind during efforts to optimize stellarator equilibria at reactor-relevant β values. Lastly, the fact that in the present simulations achieving saturation depends critically on $\beta_{\text{crit}}^{\text{KBM}}(k_y = k_y^{\text{min}})$, it is possible that the value of $\rho^\star = \rho_s/a$ – and thus the KBM threshold at $n = 1$ – of a low-magnetic-shear confinement device may affect the achievable plasma β. However, future investigation will need to determine whether this effect survives in more realistic simulation frameworks, in particular when retaining global profile effects.

Acknowledgements

The authors thank K. Aleynikova, M. Kotschenreuther and T.B. Cote for fruitful discussions.

Editor Paolo Ricci thanks the referees for their advice in evaluating this article.

https://doi.org/10.1017/S0022377821000581 Published online by Cambridge University Press

Funding

This work was supported by the US Department of Energy, Office of Science, Fusion Energy Sciences (award numbers DE-FG02-93ER54222, DE-FG02-04ER54742, DE-FG02-89ER53291 and DE-FG02-99ER54546). Computing time was provided through the National Energy Research Scientific Computing Center, a DOE Office of Science User Facility (grant number DE-AC02-05CH11231).

Declaration of interests

The authors report no conflict of interest.

REFERENCES

ALEYNIKOVA, K. & ZOCCO, A. 2017 Quantitative study of kinetic ballooning mode theory in simple geometry. *Phys. Plasmas* **24**, 092106.

ALEYNIKOVA, K., ZOCCO, A., XANTHOPOULOS, P., HELANDER, P. & NÜHRENBERG, C. 2018 Kinetic ballooning modes in tokamaks and stellarators. *J. Plasma Phys*. **84**, 745840602.

ANTONSEN, T.M. JR., Drake, J.F., Guzdar, P.N., Hassam, A.B., Lau, Y.T., Liu, C.S. & Novakovskii, S.V. 1996 Physical mechanism of enhanced stability from negative shear in tokamaks: implications for edge transport and the L-H transition. *Phys. Plasmas* **3** (6), 2221–2223.

ANTONSEN, T.M. JR. & Lane, B. 1980 Kinetic equations for low frequency instabilities in inhomogeneous plasmas. *Phys. Fluids* **23**, 1205–1214.

BALL, J., BRUNNER, S. & AJAY, C.J. 2020 Eliminating turbulent self-interaction through the parallel boundary condition in local gyrokinetic simulations. *J. Plasma Phys*. **86** (2), 905860207.

BOOZER, A.H. 1983 Transport and isomorphic equilibria. *Phys. Fluids* **26** (2), 496–499.

BRIZARD, A.J. & HAHM, T.S. 2007 Foundations of nonlinear gyrokinetic theory. *Rev. Mod. Phys*. **79** (2), 421–468.

CANIK, J.M., ANDERSON, D.T., ANDERSON, F.S.B., LIKIN, K.M., TALMADGE, J.N. & ZHAI, K. 2007 Experimental demonstration of improved neoclassical transport with quasihelical symmetry. *Phys. Rev. Lett*. **98** (8), 085002.

CHENG, C.Z. 1982 Kinetic theory of collisionless ballooning modes. *Phys. Fluids* **25**, 1020–1026.

CHEN, W., MA, R.R., LI, Y.Y., SHI, Z.B., DU, H.R., JIANG, M., YU, L.M., YUAN, B.S., LI, Y.G., YANG, Z.C., *et al.* 2016 Alfvénic ion temperature gradient activities in a weak magnetic shear plasma. *Europhys. Lett*. **116**, 45003.

CHEN, W., YU, D.L., MA, R.R., SHI, P.W., LI, Y.Y., SHI, Z.B., DU, H.R., JI, X.Q., JIANG, M., YU, L.M., *et al.* 2018 Kinetic electromagnetic instabilities in an ITB plasma with weak magnetic shear. *Nucl. Fusion* **58**, 056004.

CONNOR, J.W., HASTIE, R.J. & TAYLOR, J.B. 1978 Shear, periodicity, and plasma ballooning modes. *Phys. Rev. Lett*. **40**, 396–399.

COPPI, B. 1965 'Universal' instabilities from plasma moment equations. *Phys. Lett*. **14** (3), 172–174.

COPPI, B., ROSENBLUTH, M.N. & SADGEEV, R.Z. 1967 Instabilities due to temperature gradients in complex magnetic field configurations. *Phys. Fluids* **10** (3), 582–587.

DONG, J.Q., GUZDAR, P.N. & LEE, Y.C. 1987 Finite beta effects on ion temperature gradient driven modes. *Phys. Fluids* **30**, 2694–2702.

FABER, B.J., PUESCHEL, M.J., PROLL, J.H.E., XANTHOPOULOS, P., TERRY, P.W., HEGNA, C.C., WEIR, G.M., LIKIN, K.M. & TALMADGE, J.N. 2015 Gyrokinetic studies of trapped electron mode turbulence in Helically Symmetric eXperiment stellarator. *Phys. Plasmas* **22** (7), 072305.

FABER, B.J., PUESCHEL, M.J., TERRY, P.W., HEGNA, C.C. & ROMAN, J.E. 2018 Stellarator microinstabilities and turbulence at low magnetic shear. *J. Plasma Phys*. **84** (5), 905840503.

GATES, D.A., ANDERSON, D.T., ANDERSON, F.S.B., ZARNSTORF, M., SPONG, D.A., WEITZNER, H., NEILSON, G.H., RUZIC, D.N., ANDRUCZYK, D., HARRIS, J.H., *et al.* 2018 Stellarator research opportunities: a report on the National Stellarator Coordinating Committee. *J. Fusion Energy* **37** (1), 51–94.

GREENE, J.M. & CHANCE, M.S. 1981 The second region of stability against ballooning modes. *Nucl. Fusion* **21**, 453–464.

GRIMM, R.C., GREENE, J.M. & JOHNSON, J.L. 1976 Computation of the magnetohydrodynamic spectrum in axisymmetric toroidal confinement systems. *Meth. Comput. Phys.* **16**, 253–280.

HALL, L.S. & MCNAMARA, B. 1975 Three-dimensional equilibrium of the anisotropic, finite-pressure guiding-center plasma: theory of the magnetic plasma. *Phys. Fluids* **18** (5), 552–565.

HEGNA, C.C., TERRY, P.W. & FABER, B.J. 2018 Theory of ITG turbulent saturation in stellarators: identifying mechanisms to reduce turbulent transport. *Phys. Plasmas* **25** (2), 022511.

HIROSE, A. & ELIA, M. 1996 Kinetic ballooning mode with negative shear. *Phys. Rev. Lett.* **76** (4), 628–631.

HIROSE, A., ZHANG, L. & ELIA, M. 1995 Ion temperature gradient-driven ballooning mode in tokamaks. *Phys. Plasmas* **2**, 859–875.

HIRSCH, M., BALDZUHN, J., BEIDLER, C., BRAKEL, R., BURHENN, R., DINKLAGE, A., EHMLER, H., ENDLER, M., ERCKMANN, V., FENG, Y., *et al.* 2008 Major results from the stellarator Wendelstein 7-AS. *Plasma Phys. Control. Fusion* **50**, 053001.

HIRSHMAN, S.P., VAN RIJ, W.I. & MERKEL, P. 1986 Three-dimensional free boundary calculations using a spectral Green's function method. *Comput. Phys. commun.* **43** (1), 143–155.

HORTON, W. JR., Choi, D.-I. & Tang, W.M. 1981 Toroidal drift modes driven by ion temperature gradients. *Phys. Fluids* **24** (6), 1077–1085.

ISHIZAWA, A., KISHIMOTO, Y., WATANABE, T.-H., SUGAMA, H., TANAKA, K., SATAKE, S., KOBAYASHI, S., NAGASAKI, K. & NAKAMURA, Y. 2017 Multi-machine analysis of turbulent transport in helical systems via gyrokinetic simulation. *Nucl. Fusion* **57**, 066010.

ISHIZAWA, A., MAEYAMA, S., WATANABE, T.-H., SUGAMA, H. & NAKAJIMA, N. 2013 Gyrokinetic turbulence simulations of high-beta tokamak and helical plasmas with full-kinetic and hybrid models. *Nucl. Fusion* **53**, 053007.

ISHIZAWA, A., URANO, D., NAKAMURA, Y., MAEYAMA, S. & WATANABE, T.-H. 2019 Persistence of ion temperature gradient turbulent transport at finite normalized pressure. *Phys. Rev. Lett.* **123** (2), 025003.

JARMÉN, A., ANDERSON, J. & MALINOV, P. 2015 Effects of parallel ion motion on electromagnetic toroidal ion temperature gradient modes in a fluid model. *Phys. Plasmas* **22** (8), 082508.

JENKO, F. 2000 Massively parallel Vlasov simulation of electromagnetic drift-wave turbulence. *Compur. Phys. Commun.* **125**, 196–209.

KADOMTSEV, B.B. & POGUTSE, O.P. 1971 Trapped particles in toroidal magnetic systems. *Nucl. Fusion* **11**, 67–92.

KIM, J.Y., HORTON, W. & DONG, J.Q. 1993 Electromagnetic effect on the toroidal ion temperature gradient mode. *Phys. Fluids* B **5**, 4030–4039.

KOTSCHENREUTHER, M. 1986 Compressibility effects on ideal and kinetic ballooning modes and elimination of finite Larmor radius stabilization. *Phys. Fluids* **29** (9), 2898–2913.

MAEYAMA, S., ISHIZAWA, A., WATANABE, T.-H., NAKAJIMA, N., TSUJI-LIO, S. & TSUTSUI, H. 2013 Numerical techniques for parallel dynamics in electromagnetic gryokinetic Vlasov simulations. *Comput. Phys. Commun.* **184** (11), 2462–2473.

MCKINNEY, I.J., PUESCHEL, M.J., FABER, B.J., HEGNA, C.C., TALMADGE, J.N., ANDERSON, D.T., MYNICK, H.E. & XANTHOPOULOS, P. 2019 A comparison of turbulent transport in a quasi-helical and a quasi-axisymmetric stellarator. *J. Plasma Phys.* **85**, 905850503.

MIKHAILOV, M.I., SHAFRANOV, V.D., SUBBOTIN, A.A., YU ISAEV, M., NÜHRENBERG, J., ZILLE, R. & COOPER, W.A. 2002 Improved α-particle confinement in stellarators with poloidally closed contours of the magnetic field strength. *Nucl. Fusion* **42**, L23–L26.

MYNICK, H.E. 2006 Transport optimization in stellarators. *Phys. Plasmas* **13** (5), 058102.

MYNICK, H.E., POMPHREY, N. & XANTHOPOULOS, P. 2010 Optimizing stellarators for turbulent transport. *Phys. Rev. Lett.* **105** (9), 095004.

NEILSON, G.H., ZARNSTORFF, M.C., LYON, J.F. & THE NCSX TEAM 2002 Quasi-symmetry in stellarator research 5. Status of physics design of quasi-axisymmetry stellarators 5.1 Physics design of the National Compact Stellarator Experiment. *J. Plasma Fusion Res.* **78** (3), 214–219.

NÜHRENBERG, J. & ZILLE, R. 1988 Quasi-helically symmetric toroidal stellarators. *Phys. Lett.* A **129** (2), 113–117.

OBIKI, T., SANO, F., WAKATANI, M., KONDO, K., MIZUUCHI, T., HANATANI, K., NAKAMURA, Y., NAGASAKI, K., OKADA, H, NAKASUGA, M., *et al.* 2000 Goals and status of Heliotron-J. *Plasma Phys. Control. Fusion* **42**, 115–1164.

PALUMBO, D. 1968 Some considerations on closed configurations of magnetohydrostatic equilibrium. *Nuovo Cimento* B **53**, 507–511.

PEARLSTEIN, L.D. & BERK, H.L. 1969 Universal eigenmode in a strongly sheared magnetic field. *Phys. Rev. Lett*. **23** (5), 220–222.

PUESCHEL, M.J., DANNERT, T. & JENKO, F. 2010 On the role of the numerical dissipation in gyrokinetic Vlasov simulations of plasma microturbulence. *Comput. Phys. Commun*. **181** (8), 1428–1437.

PUESCHEL, M.J., HATCH, D.R., ERNST, D.R., GUTTENFELDER, W., TERRY, P.W., CITRIN, J. & CONNOR, J.W. 2019 On microinstabilities and turbulence in steep-gradient regions of fusion devices. *Plasma Phys. Control. Fusion* **61** (3), 034002.

PUESCHEL, M.J. & JENKO, F. 2010 Transport properties of finite-β microturbulence. *Phys. Plasmas* **17**, 062307.

PUESCHEL, M.J., JENKO, F., TOLD, D. & BUCHNER, J. 2011 Gyrokinetic simulations of magnetic reconnection. *Phys. Plasmas* **18** (11), 112102.

PUESCHEL, M.J., KAMMERER, M. & JENKO, F. 2008 Gyrokinetic turbulence simulations at high plasma beta. *Phys. Plasmas* **15**, 102310.

PU, Y.-K. & MIGLIUOLO, S. 1985 Finite beta stabilization of the kinetic ion mixing mode. *Phys. Fluids* **28**, 1722–1726.

RODRÍGUEZ, E., HELANDER, P. & BHATTACHARJEE, A. 2020 Necessary and sufficient conditions for quasisymmetry. *Phys. Plasmas* **27** (6), 062501.

ROSS, D.W. & MAHAJAN, S.M. 1978 Are drift-wave eigenmodes unstable? *Phys. Rev. Lett*. **40** (5), 324–327.

RUDAKOV, L.I. & SAGDEEV, R.Z. 1961 On the instability of a nonuniform rarefied plasma in a strong magnetic field. *Dokl. Akad. Nauk SSR* **138** (3), 581–583.

SNYDER, P.B. 1999 Gyrofluid theory and simulation of electromagnetic turbulence and transport in tokamak plasmas. *Princeton University.* PhD thesis.

SNYDER, P.B., HAMMETT, G.W., BEER, M.A. & DORLAND, W. 1999 Simulations of electromagnetic turbulence and transport in tokamak plasmas. In *Proc. 26th EPS Conf. on Contr. Fusion and Plasmas Physics*, Europhysics Conference Abstracts (ECA) series 23J, p. 1685.

STRAUSS, H.R. 1979 Finite beta trapped electron fluid mode. *Phys. Fluids* **22**, 1079–1081.

TANG, W.M. 1978 Microinstability theory in tokamaks. *Nucl. Fusion* **18** (8), 1089–1160.

WHELAN, G.G., PUESCHEL, M.J. & TERRY, P.W. 2018 Nonlinear electromagnetic stabilization of plasma microturbulence. *Phys. Rev. Lett*. **120**, 175002.

WHELAN, G.G., PUESCHEL, M.J., TERRY, P.W., CITRIN, J., MCKINNEY, I.J., GUTTENFELDER, W. & DOERK, H. 2019 Saturation and nonlinear electromagnetic stabilization of ITG turbulence. *Phys. Plasmas* **26** (8), 082302.

WOLF, R.C., ALONSO, A., ÄKÄSLOMPOLO, S., BALDZUHN, J., BEURSKENS, M., BEIDLER, C.D., BIEDERMANN, C., BOSCH, H.-S., BOZHENKOV, S., BRAKEL, R., *et al.* 2019 Performance of Wendelstein 7-X stellarator plasmas during the first divertor operation phase. *Phys. Plasmas* **26**, 082504.

XANTHOPOULOS, P., COOPER, W.A., JENKO, F., TURKIN, Y., RUNOV, A. & GEIGER, J. 2009 A geometry interface for gyrokinetic microturbulence investigations in toroidal configurations. *Phys. Plasmas* **16** (8), 082303.

XANTHOPOULOS, P. & JENKO, F. 2007 Gyrokinetic analysis of linear microinstabilities for the stellarator Wendelstein 7-X. *Phys. Plasmas* **14** (4), 042501.

XANTHOPOULOS, P., MYNICK, H.E., HELANDER, P., TURKIN, Y., PLUNK, G.G., JENKO, F., GÖRLER, T., TOLD, D., BIRD, T. & PROLL, J.H.E. 2014 Controlling turbulence in present and future stellarators. *Phys. Rev. Lett*. **113** (15), 155011.

YU ISAEV, M., NÜHRENBERG, J., MIKHAILOV, M.I., COOPER, W.A., WATANABE, K.Y., YOKOYAMA, M., YAMAZAKI, K., SUBBOTIN, A.A. & SHAFRANOV, V.D. 2003 A new class of quasi-omnigenous configurations. *Nucl. Fusion* **43**, 1066–1071.

ZONCA, F., CHEN, L., DONG, J.Q. & SANTORO, R.A. 1999 Existence of ion temperature gradient driven shear Alfvén instabilities in tokamaks. *Phys. Plasmas* **6**, 1917–1924.

https://doi.org/10.1017/S0022377821000581 Published online by Cambridge University Press